Trapping of electrons and $^{40}Ca^{+}$ ions in a dual-frequency Paul trap

Vladimir Mikhailovskii [1,2,3,*] Natalija Sheth [1,2,3,*] Guofeng Qu [4,1,2,†] Michal Hejduk [5] Niklas Vilhelm Lausti [5] K. T. Satyajith [6] Christian Smorra,[3,‡] Günther Werth,[3] Neha Yadav [7] Qian Yu [7] Clemens Matthiesen [7,§] Hartmut Häffner [7] Ferdinand Schmidt-Kaler [3] Hendrik Bekker [1,2,3] and Dmitry Budker [1,2,3,7]

[1]*Helmholtz-Institut Mainz, 55128 Mainz, Germany*

[2]*GSI Helmholtzzentrum für Schwerionenforschung GmbH, 64291 Darmstadt, Germany*

[3]*QUANTUM, Institut für Physik, Johannes Gutenberg-Universität, 55128 Mainz, Germany*

[4]*School of Physics, Northeast Normal University, Changchun 130024, Jilin, China*

[5]*Faculty of Mathematics and Physics, Charles University, Prague 8, Czech Republic*

[6]*Delta Q, IMJ Institute of Research and Department of Basic Science and Humanities, Moodalkatte Institute of Technology, Moodalkatte, Karnataka 576217, India*

[7]*Department of Physics, University of California, Berkeley, California 94720-7300, USA*

(Received 28 August 2025; revised 7 January 2026; accepted 30 January 2026; published 1 April 2026)

We demonstrate the operation of a dual-frequency Paul trap and characterize its performance by storing either electrons or calcium ions while simultaneously applying two quadrupole fields which oscillate at $\Omega_{\text{fast}} = 2\pi \times 1.6$ GHz and $\Omega_{\text{slow}} = 2\pi \times 2$ MHz. The particles are loaded and stored in the trap under various conditions, followed by detection employing an electron multiplier tube. We find that tens of electrons or ions can be trapped for up to 10 ms and a small fraction remains trapped even after hundreds of milliseconds with no further signs of loss on this timescale. During dual-frequency operation we find that while the number of trapped electrons rapidly decreases with the increase of the Ω_{slow} field amplitude, the number of trapped ions shows no dependence on the Ω_{fast} field amplitude, as supported by our extensive numerical simulations. We aim to use a similar trap for synthesizing antihydrogen from antiprotons and positrons. Accordingly, we discuss open challenges such as the cotrapping of oppositely charged species and difficulties related to trap material and manufacturing techniques.

DOI: 10.1103/q5kr-5dp7

I. INTRODUCTION

Radio-frequency (rf) Paul traps are among the most common traps in the field of atomic and molecular physics due to their reliability and excellent optical access. Remarkably, they allow for the cotrapping of oppositely charged particles [1]. In 1995, Dehmelt proposed the use of a dual-frequency Paul trap for the synthesis of antimolecular hydrogen from cotrapped antiprotons and positrons [2]. More recently, some of us modeled these particle orbits in such a device [3], as has also been done for different ion species by others [4–6]. In the present work, we demonstrate an experimental realization of a dual-frequency Paul trap as a prototype for future cotrapping of antiprotons and positrons. In our antimatter-on-a-chip (AMOC) project, we aim to study interactions between matter and antimatter and, ultimately, to produce and study antihydrogen in a tabletop experiment in our laboratory. Whereas current methods to synthesize antihydrogen involve dynamically merging two particle clouds, resulting in a limited interaction time [7–9], storing oppositely charged particles in the same volume allows, in principle, for arbitrarily long interaction time.

CERN is currently the only place where cold antiprotons can be obtained, but the baryon antibaryon symmetry experiment-transportable penning trap (BASE-STEP) [10,11] and antiproton unstable matter annihilation (PUMA) collaborations [12] are developing methods to transport them to other facilities using Penning traps. We envision that, with these novel tools and techniques, high-precision antimatter research will become commonplace in laboratories around the world, enabling a more diverse range of experiments and applications. With this in mind, we are developing an rf trap that can be loaded with antiprotons from a transportable Penning trap and positrons from a local source. There are challenges with this approach, such as injecting charged particles from external sources into the center of the rf trap and the lack of direct means to laser cool fundamental particles. We plan to overcome these challenges by employing techniques similar to those used for sympathetic cooling of externally produced highly charged ions in a cryogenic rf trap [13] or, potentially, via image-current detection and cooling of electrons [14,15]. Sympathetic cooling of positrons using Be^{+} ions at antihydrogen laser physics apparatus was very recently shown to lead to significantly enhanced production rates of antihydrogen [16]. We also note that a combined rf Paul-Penning trap that is potentially usable for antihydrogen synthesis was demonstrated in 1995, but it saw limited use [17,18]. And the gravitational

*These authors contributed equally to this work.

†Contact author: quguofeng@scu.edu.cn

‡Present address: Lehrstuhl für Quantentechnologie und Fundamentalphysik, Heinrich-Heine-Universität Düsseldorf, 40225 Düsseldorf, Germany.

§Present address: Oxford Ionics, Oxford OX5 1PF, United Kingdom.

behaviour of anti hydrogen at rest (GBAR) collaboration aims to develop an rf Paul trap for storage and cooling antihydrogen anions [19].

Antimatter research is at the frontier of the search for physics beyond the standard model because of one of the key mysteries of modern physics: the observed asymmetry between matter and antimatter in the known universe [20]. High-resolution spectroscopy of antihydrogen is a promising approach [21–23]. High-precision measurements and comparisons of the fundamental properties of matter and antimatter are also used to address this challenge, in which the mass [24–26], charge [27], and magnetic moments [28,29] are investigated. In the latter case, the BASE-STEP experiment is specifically being developed to perform such measurements on antiprotons away from the electromagnetically noisy environment at the antiproton decelerator, limiting the achievable precision [10]. Currently, these antihydrogen and antiproton experiments are exclusively performed in Penning traps due to the ease and early demonstration of injection from antiproton decelerators [30] and in-trap sympathetic cooling with cold electrons [31]. Our dual-frequency Paul trap will allow for complementary measurements that are difficult in a Penning trap, such as laser spectroscopy of bound states between antimatter particles with very different charge-to-mass ratios and of matter-antimatter bound states [32,33].

In the present study, we develop an rf trap for cotrapping electrons and atomic ions which act as analogs for positrons and antiprotons. At the current stage of AMOC we prefer to use these easily accessible particles because, to a large degree, only their charge-to-mass ratio q/m affects the trap stability. In other words, the results for electrons can be applied to positrons simply by inverting the polarity of dc electrodes. And instead of (anti)protons we use heavier $^{40}Ca^{+}$ ions coming from the same source as the electrons. Due to the very different ratios q/m of electrons and ions, two frequencies have to be applied for stable trapping. Predominantly theoretical studies have been performed for this in the case of ions trapped in a dual-frequency field [4–6]. More recently, cotrapping of a nanoparticle with an atomic ion, where q/m differed by a factor of 10^6, was experimentally demonstrated [34]. In this work, we demonstrate the successful trapping of electrons or much heavier Ca^{+} ions in our dual-frequency rf trap and investigate the relevant properties of this device as a pathway to cotrapping these species.

Trapping electrons employing an rf trap is challenging due to the need for gigahertz- instead of megahertz-frequency fields and also the absence of laser-cooling methods and laser-induced fluorescence detection techniques. A few groups have managed to overcome these challenges [15,17,35] with a range of applications, such as quantum information and computation [14,36–38]. Applying a second frequency to these devices requires careful tuning of the frequency and amplitude to ensure continued stable trapping of the electrons. Moreover, the application of such a second frequency poses practical challenges due to the common use of single-frequency resonators to enhance the trapping field.

This paper is organized as follows: Starting with the description of our experimental setup, we then develop the dual-rf trap theory applicable to our trap geometry to obtain predictions for the regions of stability. Subsequently, we describe the experimental results from loading and trapping electrons or $^{40}Ca^{+}$ ions while applying either one or two rf fields. We characterize the trapping time distribution and study trapping stability. Finally, we sketch future plans for improved trap designs.

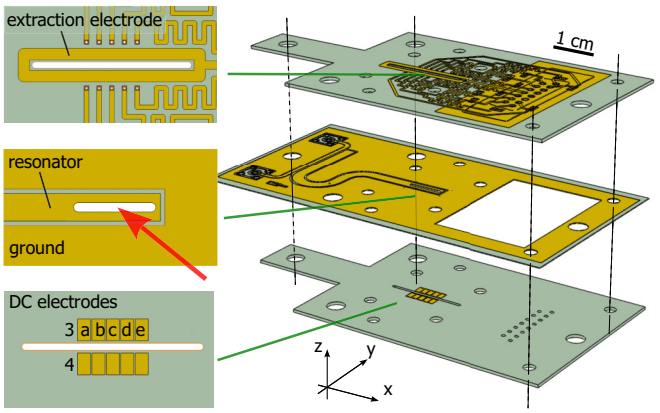

FIG. 1. Exploded-view drawing of the trap PCBs based on [35]. The central PCB features a curved resonator to provide the quadrupole field in the slot shown in the middle inset. The red arrow indicates the position of trapped particles. The identical top and bottom PCBs have 10 dc electrodes on the side facing the central board, as shown in the bottom inset, and an extraction electrode facing away from the center, as shown in the top inset.

II. EXPERIMENTAL SETUP

Here we describe the technical details of our setup, including the trap, particle-loading method, and detection scheme. Depending on the trapped species and purpose of the measurement, different sets of rf, dc, and extraction voltages are applied.

A. Trap design

Our linear segmented Paul trap is assembled from three printed circuit boards (PCBs) on a Rogers 4003C substrate, and they are separated by 1.27 mm using ceramic spacers (see Fig. 1). The thickness of the central board is 0.2 mm, and that of the others is 0.8 mm. The rf electrode consists of a capacitively coupled coplanar waveguide $\lambda/2$ resonator on the central PCB [35]. It is shorted to ground at the center, has a resonance frequency of $\Omega_{\text{fast}} = 2\pi \times 1.6$ GHz, and has a Q factor of 25. In a 9.0-mm-long and 0.9-mm-wide slot at the end of the resonator it generates a quadrupole field in the yz plane used to trap electrons. The top and bottom boards have 21.0-mm-long and 0.9-mm-wide slots parallel to the central slot that allow for optical access to the trap region. Those boards feature 10 segmented dc electrodes symmetrically distributed on both sides of the slot on the PCB side facing the central board. Each block of five dc electrodes is labeled from a to e starting from the coupling side of the resonator. The outside surfaces of both PCBs also contain a single electrode around the slots used to extract particles. The assembly is placed at the center of a vacuum chamber, as shown in Fig. 2. The chamber is pumped by an Agilent

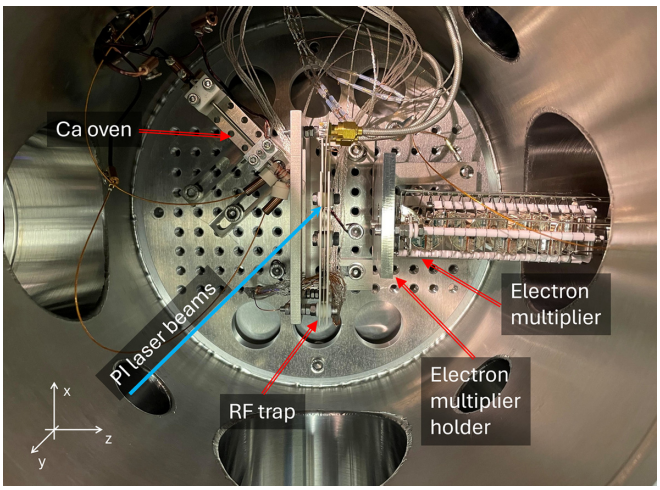

FIG. 2. Top-down view of the experimental setup in the vacuum chamber. The trap PCBs, labeled "RF trap," are seen from the side.

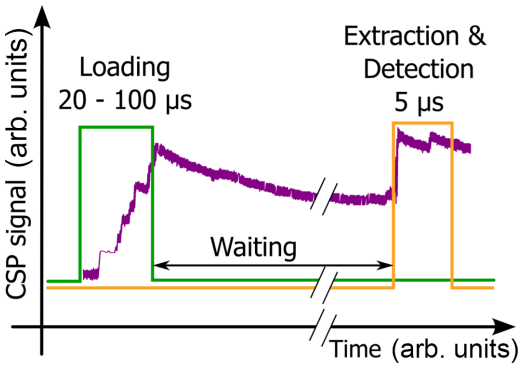

FIG. 3. Timing sequence of a typical measurement cycle. Green line: gate for the AOM driver of the photoionizing 390 -nm laser beam. Orange line: extraction voltage. Purple: signal from the charge-sensitive preamplifier in the case of electron detection. For ion detection the overall scheme is similar.

TwissTorr 304 turbopump and a Saes NEXTorr Z 100 getter pump to a base pressure on the order of 10^{-10} hPa.

Typically, an rf field with approximately 2 W of power is applied at the resonator frequency Ω_{fast} to the in-coupling electrode, which results in the quadrupole field in the yz plane inside the slot of the resonator. To confine electrons in the x direction, the a and e dc electrodes are biased by -6 V, the b and d electrodes are biased by -2 V, while the c and extraction electrodes are kept at ground potential.

To trap ions, we apply Ω_{slow} to one pair of diagonally opposite c electrodes while keeping the other pair grounded. This generates another quadrupole field in the yz plane with its center coinciding with the field generated by the resonator. Confinement in the x direction is again achieved using the remaining dc electrodes, in this case by applying positive voltages: The a and e electrodes are biased to $+5$ V, b and d are biased at $+3$ V, and the extraction electrode is grounded.

Since trapping electrons and $^{40}Ca^{+}$ ions requires opposite polarities on the dc electrodes, simultaneous cotrapping is not expected with the present setup. Instead, we focus on studying the rf trapping conditions, specifically, how one species can be confined in a dual-frequency field that would also be suitable for trapping the other. In future work we plan to use a three-dimensional rf Paul trap without dc electrodes. Single-frequency versions of such devices have been used to cotrap cations and anions for molecular reaction studies (e.g., [39]).

B. Measurement sequence

Most of the measurements presented here consist of three steps: loading electrons or ions into the trap, storing them for a defined waiting time, and then extracting them for detection, as shown in Fig. 3. Electrons and ions are loaded into the trap by photoionization of calcium atoms. To this end, an atomic oven emits a Ca beam at a 45° angle with respect to the PCB surfaces so that it crosses the center of the trap. We employ the two-step photoionization scheme of ^{40}Ca [40], where a laser beam at 423 nm is used to resonantly drive the 4^1S_0–4^1P_1 transition in neutral Ca, and the second laser beam at 390 nm is used for ionizing from the 4^1P_1 state to near the continuum. This results in electrons and ions with sufficiently low energy for trapping. Both laser beams are coupled into the same single-mode fiber for good spatial alignment, as confirmed by using a CCD camera to determine the beam properties. Subsequently, they are sent into the trap chamber through a viewport at a right angle to the calcium beam (see Fig. 2). At the trap center, the laser beams overlap and have a power of approximately 1 mW, and the beam diameters are 20 and 80 μm for the laser beams at 390 and 423 nm, respectively.

During a measurement cycle, the atomic beam, 423-nm laser beam, and rf field remain on. The 390-nm beam is switched on only during the loading period by means of a single-pass acousto-optic modulator (AOM). Subsequently, the charged particles are stored in the trap for a defined waiting time which we vary from microseconds to, maximally, a second. This step ends with the application of a $+1$-V extraction pulse for 5 μs to the c electrodes (in the case of electrons) and -1 V to the b and d electrodes (in the case of ions) on the side facing the detector and to the extraction electrode on the same side. Here we use a Hamamatsu R596 electron multiplier tube (EMT) placed at a distance of 3 cm from the trap. We apply $+140$ V (in the case of electrons) or -500 V (for ions) to the front EMT holder to enhance collection efficiency without distorting the potential inside the trap according to finite-element modeling. A high voltage of 2000 V is applied across the EMT, resulting in a gain of approximately 10^6.

The EMT output is amplified using a charge-sensitive preamplifier (CSP; model ORTEC 142PC) with a feedback capacitor of 0.1 pF. The resulting signal is a voltage pulse with a nanoseconds rising edge and a slow decay of tens of microseconds; the amplitude of the pulses is proportional to the number of charges. Pulses are digitized using a CAEN DT5770 digitizer. Applying the Ω_{slow} field to the central electrodes for ion trapping introduces significant electronic pickup in the detection system. To avoid this, we include a notch filter between the CSP and digitizer, with its central frequency at 2 MHz. The digitizer is able to detect incoming pulses either continuously, using an internal trigger, or at defined time points, using an external trigger.

To calibrate the EMT and to optimize various parameters, such as the EMT holder potential, we use continuous detection. In this case, the rf field is off, and the signal is due to electrons or ions (depending on the EMT potentials) generated by photoionization of calcium atoms. For trapping experiments when the rf field is on, the digitizer is triggered externally, so the detection window coincides with the application of the extraction pulse to the trap electrodes. During the loading time the EMT signal shows stepwise increases corresponding to overlapping fast-rise pulses at the output of the CSP, as shown in Fig. 3. These pulses are caused by charged particles that are not trapped and leave this region soon after production. During the measurement cycle, noise electrons produced by the hot atomic oven or by field emission from the trap electrodes may also be detected at random times. Their number does not exceed 5% of all detection events. When the extraction voltage is applied, we observe a sharp increase in the signal. In comparison to the stepwise voltage increases during loading, this appears as a single pulse, suggesting that the detected particles arrive as a bunch due to their simultaneous extraction from the trap. Such behavior is observed only when all necessary components—the rf field, dc voltages, and properly aligned laser beams—are applied together. The appearance of this signal and its time correlation with the measurement cycle serve as primary evidence of successful particle trapping.

To measure the number of trapped particles, we repeat the sequence 10^3–10^4 times and average over CSP pulses detected by the digitizer during the extraction pulses. Then the average height of the CSP pulses is converted to the average number of particles using the calibration procedure described in the Appendix. The uncertainty in the average number of particles is estimated from the CSP pulse-amplitude histogram.

III. THEORY OF DUAL-FREQUENCY PAUL TRAPS

We briefly review the theory of general dual-frequency Paul traps and subsequently apply it to our trap geometry.

A. General dual-frequency trap

The amplitude U and angular frequency Ω of a field necessary for trapping charged particles is determined by their charge-to-mass ratio q/m [41]. For cotrapping species for which this ratio differs roughly by an order of magnitude or more, the application of two fields is necessary. To ensure that both particle clouds are approximately the same size, the voltages $U_{\rm slow}$ and $U_{\rm fast}$ and frequencies $\Omega_{\rm slow}$ and $\Omega_{\rm fast}$ of both fields should be chosen in such a way that the spring constants κ of both species in the oscillating potential are nearly equal [4], meaning that

$$\frac{\kappa_{\rm e}}{\kappa_{\rm Ca}} = \left(\frac{U_{\rm fast}}{U_{\rm slow}}\right)^2 \left(\frac{\Omega_{\rm slow}}{\Omega_{\rm fast}}\right)^2 \left(\frac{m_{\rm Ca}}{m_{\rm e}}\right) \approx 1. \tag{1}$$

Since the mass ratio $m_{\rm Ca}/m_{\rm e}$ is about 73 000, this condition suggests that a frequency ratio $\eta := \Omega_{\rm fast}/\Omega_{\rm slow}$ on the order of 10^2 is required. This mass difference implies that the electron motion is much faster than the ion motion, meaning that the higher-frequency field $\Omega_{\rm fast}$ is required to form the quadrupole potential for the electron trap, while the slower-moving ions are confined by the lower-frequency field $\Omega_{\rm slow}$. In our measurements and modeling we fix the frequency ratio to $\eta = \Omega_{\rm fast}/\Omega_{\rm slow} = 800$, as determined by the fixed resonator frequency and that of the low-frequency notch filter. Experimentally, we probe a range of Mathieu q parameters by adjusting the amplitudes $U_{\rm slow}$ and $U_{\rm fast}$.

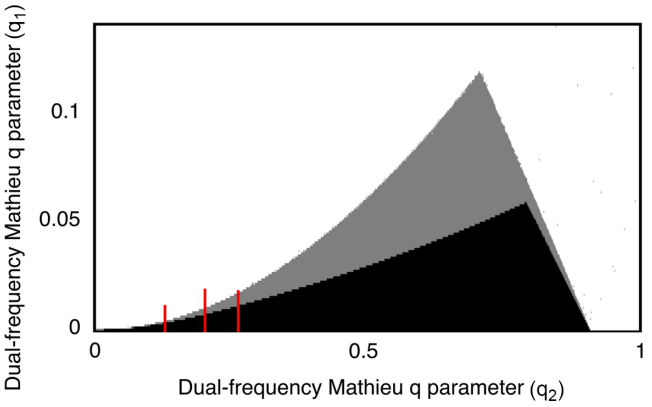

FIG. 4. Stability diagram for $\eta = 800$. The gray region represents stable sets of (q_1, q_2) for general dual-frequency traps in the y direction. Along the z direction, the signs of q_1 and q_2 flip. The black region shows the same for our trap geometry. The red lines indicate in which region we test the trapping of electrons experimentally.

The stability of particles in dual-frequency traps was studied in other works (for example, [3,5]). The time-dependent potential due to two rf fields in a quadrupole geometry can be written as

$$\Phi(t, y, z) = [U_0 + U_{\rm slow}\cos(\Omega_{\rm slow}t) + U_{\rm fast}\cos(\Omega_{\rm fast}t)]\frac{z^2 - y^2}{2r_0^2}, \tag{2}$$

where U_0 is a dc potential and r_0 is the half-distance between opposite electrodes. By introducing the dimensionless time $\tau = \Omega_{\rm fast}t/2$, the condition $\mathbf{F} = -e\,\nabla\Phi$ results in the dimensionless Mathieu equations of motion,

$$\ddot{u}(\tau) + [a_{\rm u} - 2q_1^u\cos(2\eta^{-1}\tau) - 2q_2^u\cos(2\tau)]u(\tau) = 0, \tag{3}$$

with $u = \{x, y\}$. Thereby, we define

$$a_u = 4\frac{eU_0}{mr_0^2\Omega_{\rm fast}^2} \tag{4}$$

and

$$q_{1,2}^z = -q_{1,2}^y = -2\frac{eU_{\rm slow,\,fast}}{mr_{1,2}^2\Omega_{\rm fast}^2}, \tag{5}$$

with m being the mass of the trapped particle.

Because η is a rational number, it is possible to use Floquet theory to find an analytical expression for the set of q's and a's that lead to stable trapping [3]. For this, effectively, the zeros of a matrix determinant have to be found. A graphical representation of the stability region for $\eta = 800$ and $a_u = 0$ is shown in Fig. 4. Note that this diagram is only for the stability along the y axis.

In practice, it is difficult to apply two different frequencies to the same set of electrodes. The reason is mainly that they are often driven using a resonator in order to reach sufficiently

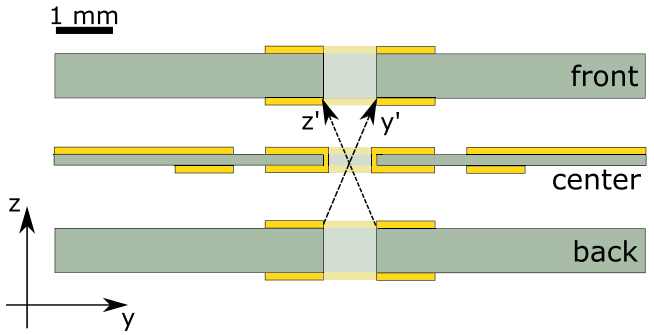

FIG. 5. Cross section in the yz plane of the trap showing the PCB substrate in gray and yellow electrodes (thickness exaggerated for visibility). The trap axes y' and z' are shown between the dc electrodes to which Ω_{fast} is applied for confining ions. Ions and electrons are trapped where y' and z' cross.

high field amplitudes, which is challenging to implement for two-frequency operation. For example, the waveguide resonator of our trap strongly damps signals below 1.6 GHz. Therefore, we use another set of electrodes to apply the low-frequency field. This has the added benefit of providing an opportunity to optimize their shape and distance r_0 for their respective frequency, which we will exploit in future traps. Moreover, using different sets of electrodes allows for an independent fine adjustment of the centers for both trapped species, if desired. In the following section, we describe the theory of our trap geometry, in which two different sets of electrodes are operated at two different frequencies.

B. Stability of orbits

While the central dc electrodes were not originally designed for rf operation and their geometry is not optimized for this purpose, the Paul-trap principle is remarkably robust. Even with flat and nonorthogonal pairs of electrodes, as shown in Fig. 5, we are able to trap ions. The resulting rf field is in the same yz plane as the field for confining electrons. To determine the equations of motion, the potential given in Eq. (2) has to be adapted to account for the nonorthogonality of the electrodes. We associate the orthogonal y and z axes with the waveguide resonator to which we apply a signal of frequency Ω_{fast}. The nonorthogonal y' and z' axes are associated with the dc electrodes to which a frequency Ω_{slow} is applied, (see Fig. 5). The angle between the two axes y and y' is $\beta = 62°$, so we can make a coordinate transformation using the constants $c_1 \coloneqq -\cos 2\beta$ and $c_2 \coloneqq \cos 4\beta / \sin 2\beta$. Therefore, the quadrupole component of the potential experienced by a particle in the trap is described by

$$\begin{aligned}\Phi(t, y, z) = U_{\text{slow}} \cos(\Omega_{\text{slow}} t) \frac{c_1 y^2 - c_1 z^2 + c_2 yz}{2r_1^2} \\ + U_{\text{fast},\,y} \cos(\Omega_{\text{fast}} t) \frac{y^2}{2r_{2,y}^2} \\ - U_{\text{fast},\,z} \cos(\Omega_{\text{fast}} t) \frac{z^2}{2r_{2,z}^2},\end{aligned} \tag{6}$$

where we take into account the different dimensions $r_{2,y/z}$ and amplitudes $U_{\text{fast},\,y/z}$ of the resonator in the y and z directions, respectively.

This potential results in a coupled motion in the y and z directions which is described by the equations of motion

$$\begin{aligned}&\ddot{y}(\tau) - \left[4c_1 q_{1,y} \cos(2\eta^{-1}\tau) + 2q_{2,y} \cos(2\tau)\right] y(\tau) \\ &+ 2c_2 q_{1,z} \cos(2\eta^{-1}\tau) z(\tau) = 0, \qquad (7a) \\ &\ddot{z}(\tau) - \left[4c_1 q_{1,z} \cos(2\eta^{-1}\tau) + 2q_{2,z} \cos(2\tau)\right] z(\tau) \\ &- 2c_2 q_{1,y} \cos(2\eta^{-1}\tau) y(\tau) = 0, \qquad (7b)\end{aligned}$$

with η and τ as defined in Sec. III A. The q parameters are now given by

$$q_{1,y} = -q_{1,z} = -2\frac{eU_{\text{slow}}}{mr_1^2\Omega_{\text{fast}}^2} \tag{8}$$

and

$$q_{2,y} = -2\frac{eU_{\text{fast},\,y}}{mr_{2,y}^2\Omega_{\text{fast}}^2}, \tag{9a}$$

$$q_{2,z} = 2\frac{eU_{\text{fast},\,,z}}{mr_{2,z}^2\Omega_{\text{fast}}^2}, \tag{9b}$$

where m is the mass of the trapped particle species.

To solve the equations of motion (7) for $u = \{y, z\}$, we employ the fourth-order Runge-Kutta method for various sets of q parameters. Using a method similar to that in [3], we introduce the stability parameter

$$S = \frac{1}{\tau_2 - \tau_1} \int_{\tau_1}^{\tau_2} u^2(\tau)\, \mathrm{d}\tau \tag{10}$$

and consider a trajectory to be stable only if $S < r_1^2$ when $\tau_1 = 0$ and $\tau_2 = 100\,000$. These parameters ensure that the average amplitude of the particle motion does not exceed the trapping volume for 200 000 periods of the Ω_{fast} field and 250 periods of the Ω_{slow} field. With this condition, we can generate stability diagrams, as shown in Fig. 4.

When comparing the stability regions of the two different geometries of dual-frequency traps, we realize that our nonorthogonal electrode design puts more constraints on the low-frequency field. While we can find stable trajectories with values of q_1 up to 0.119 for general dual-frequency traps with orthogonal electrodes, the upper limit of q_1 for our trap is only 0.06 with our geometry.

In this work, we use six distinct Mathieu q parameters. The trapping in a single-frequency rf trap is characterized by the parameter $q_e = 2eU_{\text{fast}}/m_e r_2^2 \Omega_1^2$ for electrons and the parameter $q_{\text{Ca}^+} = 2eU_{\text{slow}}/m_{\text{Ca}} r_1^2 \Omega_2^2$ for calcium ions. In the context of dual-frequency trapping, the stability of electrons is defined by the two parameters $q_{1,\,e}$ and $q_{2,\,e}$, as defined in Eqs. (8) and (9), by setting $m = m_e$. Setting $m = m_{\text{Ca}}$ results in the parameters $q_{1,\,\text{Ca}^+}$ and $q_{2,\,\text{Ca}^+}$, which describe the stability of calcium ions in the dual-frequency trap. In all cases, no distinction is made between the y and z directions since it is assumed that the absolute values are equal along both axes.

IV. EXPERIMENTAL RESULTS AND DISCUSSION

As described in Sec. II B and supported by our theoretical predictions, we successfully trapped electrons and calcium

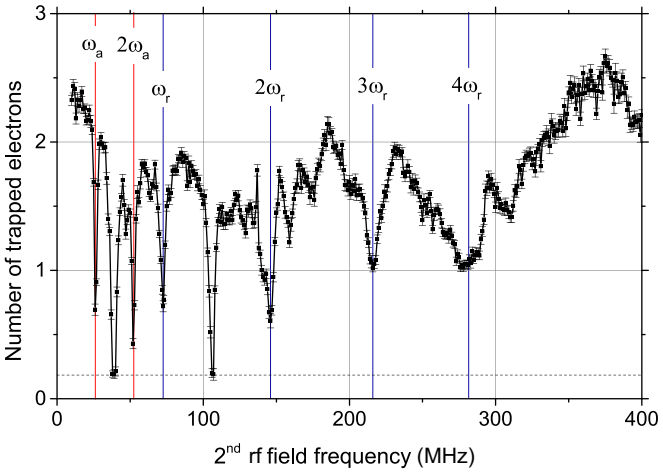

FIG. 6. Dependence of the average number of trapped electrons on the second frequency, applied to the c electrodes of the trap. The loading and waiting times were 100 and 500 μs, respectively. Ω_{fast} input power is 2.6 W, and the second rf frequency voltage is 1.5 V. The dashed line indicates the background level.

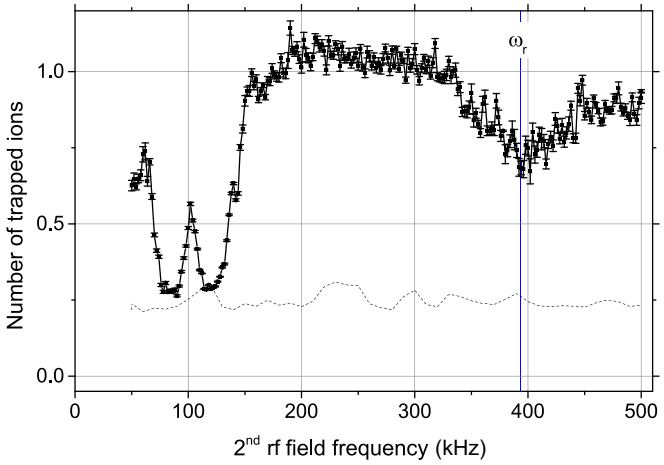

FIG. 7. Average number of extracted Ca^+ ions as a function of the second frequency, applied to the d electrode. Loading time is 100 μs, and waiting time is 1 ms. Ω_{slow} voltage amplitude is 35 V, and the second rf frequency voltage is 3 V. The dashed line indicates the background level.

ions separately. Next, we characterize the trap by studying the effects of the dual-frequency operation on the motion of trapped particles and attempt to find the optimal working point.

A. Motional frequencies of the electrons and ions

Application of a second rf field to the trapped particles can result in undesirable unstable conditions. Specifically, when the frequency of the second rf field is equal to the secular frequency ω of the particles' macromotion, its amplitude is increased, resulting in particles loss. Since we keep the Mathieu parameter $a_{y,z} = 0$, the secular frequency is related to the Mathieu q parameter through $\omega = q\Omega/2\sqrt{2}$, and observation of this effect allows us to also compare the results with the theory developed in Sec. III B.

To investigate this for electrons, we apply a second rf field to one pair of diagonally opposite c electrodes, as done when trapping ions. We scan the frequency in the range from $2\pi \times 10$ to $2\pi \times 400$ MHz in 1-MHz steps while measuring the number of extracted electrons after a waiting time of 500 μs. The resulting spectrum shown in Fig. 6 features several dips which could be due to excitation of the macromotion. To confirm this and to identify the nature of the dips, we vary the dc potential and the rf drive power: Resonances whose position shifts with dc bias are associated with axial motion, while those sensitive to the power of Ω_{fast} field are associated with radial motion. The lowest axial frequency is measured at $\omega_a = 2\pi \times 26$ MHz, and the lowest radial frequency is measured at $\omega_r = 2\pi \times 72$ MHz. Two resonances at $2\pi \times 38$ and $2\pi \times 106$ MHz show no sensitivity to either dc or rf amplitude changes and coincide with significant MHz pickup in the detection chain and dc electrodes. We therefore suspect these two features are spurious resonances of the wiring or electronics rather than motional frequencies of electrons.

To study the frequencies of ion motion inside the trap, we apply an additional rf field to one of the d electrodes of the trap. The amplitude of the corresponding voltage is 3 V, and we vary the frequency from $2\pi \times 50$ to $2\pi \times 500$ kHz while measuring how many ions on average can be extracted after 1 ms of waiting time. The results are shown in Fig. 7. As the resonance at $2\pi \times 395$ kHz shifts under the variation of the megahertz trapping voltage and has no sensitivity to dc variation, it is attributed to the radial motion of Ca^+ ions. Two dips at $2\pi \times 80$ and $2\pi \times 120$ kHz are insensitive to variations of both dc electrode potentials and the Ω_{slow} voltage. Therefore, we again attribute them to spurious resonances not related to the secular motion of ions.

B. Stability of particle orbits

To determine the stability of the orbits on which trapped particles move, we studied the evolution of the trapped particle number over a waiting period ranging from 10 μs up to 1 s. Results are shown in Fig. 8 for electrons and in Fig. 9 for ions. The initial number of extracted particles N_1 depends on several parameters such as loading time and field amplitude, as well as the overall quality of the trap, which is affected, for example, by the alignment of the PCBs. Subsequently, the number drops exponentially with a decay constant τ until a plateau at N_0 is reached, as described by the fitting function

$$N = N_0 + N_1 e^{-t/\tau}. \tag{11}$$

A similar behavior was previously reported with the same trap design in Berkeley and can be explained by a significant number of electrons being produced near the fringes of the trap volume. Simulations show that, depending on the phase of the rf field at the time of ionization, these electrons can reside on unstable orbits in the trap for an extended period [35]. We estimate that losses due to collisions with the background gas and atomic beam particles are negligible on the timescales studied here.

For both electrons and ions, we observe lifetimes of the initial population on the order of several milliseconds. The final population parameter N_0 includes contributions from trapped

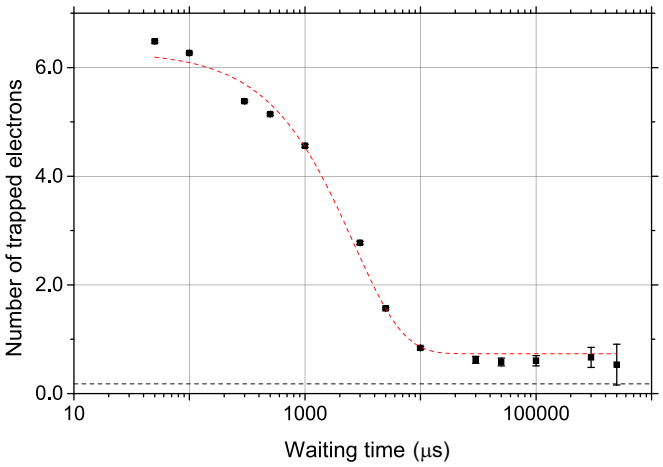

FIG. 8. Average number of extracted electrons as a function of waiting time. Loading time is 50 μs. Ω_{fast} input power is 1.2 W. The red dashed line indicates the exponential decay model of Eq. (11). The dashed line indicates the background level when the ionization lasers are blocked.

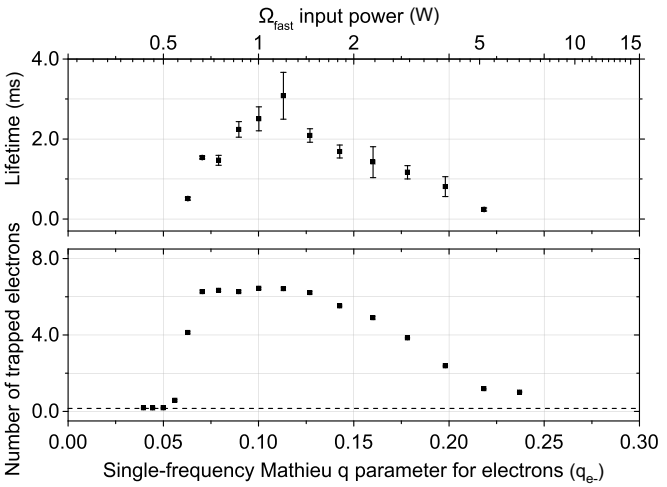

FIG. 10. Trapping efficiency versus Mathieu q_e parameter for electrons. Top: storage time of electrons τ; bottom: number of electrons N_0 extracted after 50-μs waiting time. The dashed line indicates the background level.

electrons and a small constant background due to spurious production of charged particles in the vacuum chamber. It is typically one electron per 10 loadings, as determined by blocking both laser beams while all other elements of the experiment, such as the atomic oven and the rf field, remain switched on. We find that, maximally, one particle remains in the trap after 1 s of waiting time, with no further signs of loss (see Fig 8). Therefore, this particle appears to be on a stable orbit. We attribute the initial rapid loss of particles to the existence of metastable orbits for particles generated at the fringes of the trapping volume, where anharmonic contributions to the potential become significant. Simulations performed in previous work showed that the likelihood of such metastable orbits occurring also depends on the rf phase at the time of photoionization [35].

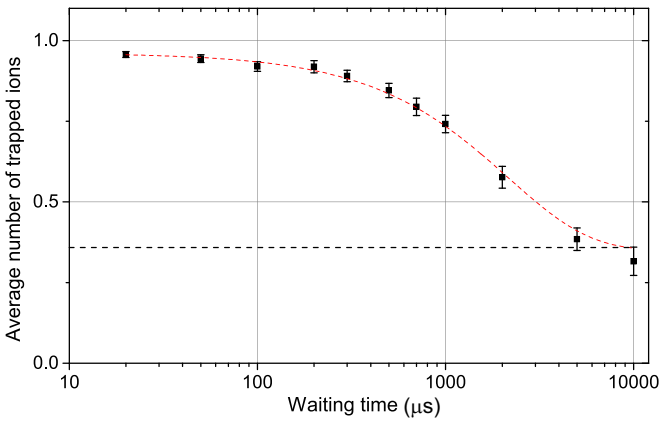

FIG. 9. Average number of extracted Ca^{+} ions as a function of waiting time. Loading time is 50 μs. Trapping field frequency $\Omega_{\text{slow}} = 2$ MHz, and voltage amplitude is 35 V. The red dashed line indicates the exponential decay. The horizontal dashed line indicates the background level when the ionization lasers are blocked.

To investigate the region of stability for electrons, we conduct a series of measurements at various amplitudes of the Ω_{fast} field. We extract two characteristics to quantify the stability of particle orbits. The first is the number of loaded electrons N_0 measured after a waiting time of 50 μs, and the second is the lifetime of electrons (see Fig. 10). Both measured characteristics show a clear dependence on the power of the Ω_{fast} field. The optimal value of the Ω_{fast} input power for trapping is found to be approximately 1.2 W, which corresponds to a q_e parameter of 0.11. Beyond this value, both the number and the lifetime of electrons drop. The lifetime curve has a sharper decline, which may indicate that at nonoptimal values of the trap drive, electrons still can be trapped but cannot be confined for a long time. The onset of instability at relatively low values of q_e can be explained by the low mass of electrons, which leads to a larger motional amplitude than that of ions at the same value of q. A similar measurement was performed for ions in the Ω_{slow} field, where only the number of initially loaded ions was measured; results are shown in Fig. 11. Here, the onset of instability occurs for $q_{Ca^+} \gtrsim 0.5$, as is typical for ions in Paul traps.

C. Trapping electrons and ions with two frequencies applied

Now that we know the optimal conditions for trapping electrons and ions in single rf fields and have ensured that the applied frequencies do not coincide with secular frequencies of the other species, we attempt to find conditions where both species can be trapped simultaneously. To this end, we trap electrons at different strengths of the Ω_{fast} field and investigate the trapping efficiency for electrons when applying the Ω_{slow} field for ion trapping on the ion-trap electrodes. Similarly, we trap Ca^{+} ions using different amplitudes of the Ω_{slow} field and investigate the trapping stability while driving the resonator at Ω_{fast}. Results are shown in Fig. 12. Even small amplitudes of the Ω_{slow} field cause a significant decrease in the number of trapped electrons, and this value drops to zero at 12 V for the Ω_{slow} voltage. A comparison to Fig. 4 shows that, ideally,

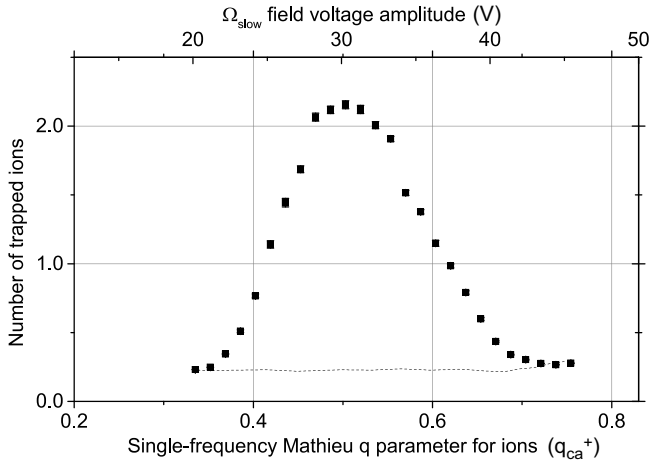

FIG. 11. Trapping efficiency versus the Mathieu q_{Ca^+} parameter for Ca^+ ions. Loading time is 100 μs, and waiting time is 50 μs. The dashed line indicates the background level.

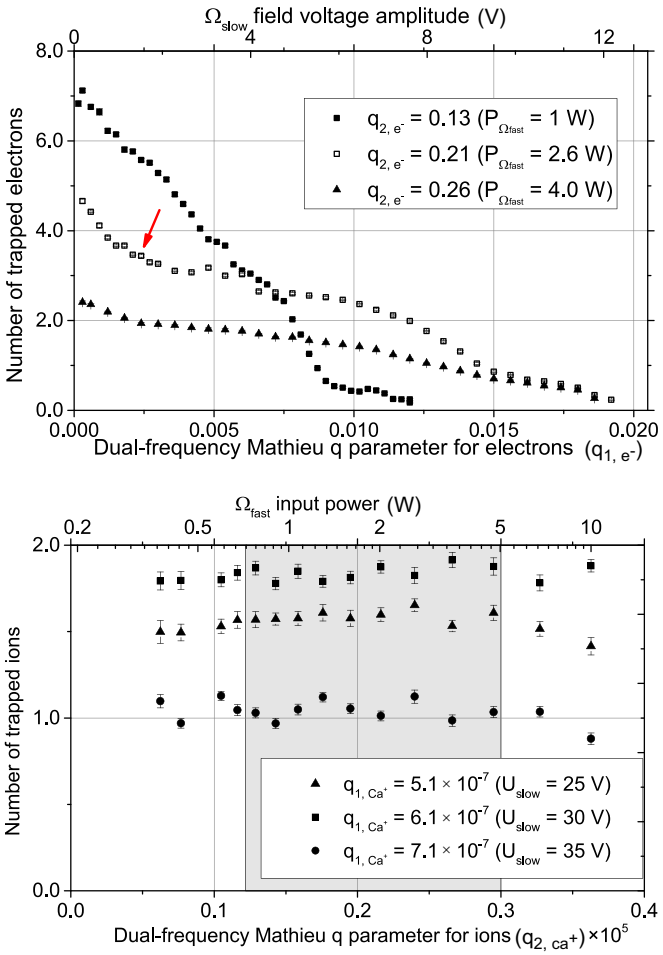

FIG. 12. Top: the dependence of the average number of trapped electrons on the amplitude of the Ω_{slow} voltage at a wait time (WT) of 50 μs. The red arrow indicates the voltage amplitude at which the frequency scan shown in Fig. 6 was acquired. Bottom: the dependence of the average number of trapped Ca^+ ions on the power of Ω_{fast} field at WT = 50 μs and WT = 500 μs. The gray area indicates the range of the Ω_{fast} input power for stable electron trapping at a single frequency.

$q_{2,e}$ should be increased to work in a region where larger amplitudes of the Ω_{slow} field can be allowed for stable trapping of electrons. But that requires the application of more power at Ω_{fast}, which would damage our trap. As indicated by the red lines in Fig. 4, stable cotrapping should theoretically be possible at the probed values of $q_{2,e}$. Imperfections in the electrode shape and alignment most likely prevent this. Specifically, our simulations are performed under the assumption of a perfect quadrupole potential, but the flat and rectangular shapes of the employed electrodes introduce higher-order terms that lead to unstable orbits [42].

The situation for ions is completely different. We keep q_{1,Ca^+} fixed and scan q_{2,Ca^+} from 0.06×10^{-5} to 0.4×10^{-5}. We find that even high voltages of the Ω_{fast} field do not affect the number of trapped ions. The different response to the second frequency field agrees with our theoretical expectations and can be explained by the mass difference between electrons and ions. While the fast oscillations of the Ω_{fast} field average to zero on the timescales of the slow motion of the ions, the slower-oscillating trapping field for ions corresponds to a quasi-dc potential for electrons.

V. CONCLUSIONS AND OUTLOOK

In this work, we demonstrated the suitability of our trap geometry for storing either electrons or ions in the same trap volume while applying two rf fields simultaneously. We observe that when operating at a single frequency, tens of electrons or ions can be stored with a storage time of several milliseconds. Typically, one electron or ion remains in the trap for at least 1 s. In the dual-frequency mode, the measured number of trapped ions does not depend on the amplitude of the Ω_{fast} field, while the number of trapped electrons decreases by approximately 10% for every 1 V increase in the Ω_{slow} voltage. This behavior is consistent with our theory and can be explained by differences in the particle masses and corresponding oscillation frequencies and amplitudes. Additionally, at the accessible Ω_{fast} power, stable trapping is sensitive to imperfections in the Ω_{slow} field which is exacerbated in our nonorthogonal electrode geometry. This further highlights the difficulties in trapping electrons in an rf trap.

To address the issues that prevent us from cotrapping electrons and ions, we are developing a next-generation trap. Misalignment of electrodes due to mechanical tolerances and thermal cycling when high rf power is applied distorts the quadrupole field. Furthermore, the surface roughness and sharp edges of PCB electrodes introduce local electric field cusps that further distort the quadrupole field so that the trap volume is reduced and heating rates are increased [42–44]. Our theoretical predictions show that the region of stability can be increased by implementing orthogonal electrodes for the megahertz field. Additionally, we aim to reduce the bare dielectric surface area of the PCBs exposed to photoelectrons and ions, which tend to accumulate static charge, thereby perturbing the trapping potential noticeably on a few-hour timescale. To address these challenges, we plan to fabricate a new trap from a more rigid material which allows the precision and stability of trap-element alignment to be improved. We also plan to minimize the exposure of dielectric surfaces by ensuring they are electrostatically shielded from the trap

center and to fabricate electrodes with smoother surfaces and gentler curvatures. All these requirements can be met with the selective-laser-etching fabrication technology used in state-of-the-art ion traps [45,46].

In future work we plan on trapping cold positrons generated in the β^+ decay of ^{22}Na that are moderated and cooled in a buffer-gas trap [47]. Cotrapping these with normal matter will allow us to pursue a rewarding scientific program, including the investigation of bound positron-atom systems [32,33]. Moreover, our experiments pave the way for synthesizing antihydrogen and molecular anti-ions from its elementary constituents by storing both positrons and antiprotons in the same rf trap volume. In this regard, the results presented here are promising because they suggest that cotrapping of antiprotons, which have a lower mass than $^{40}Ca^{+}$ ions, and positrons in rf traps seems to be achievable by careful adjustment of the lower-frequency field. This method is attractive because more refined electrode geometries will potentially allow for arbitrarily long storage and interaction times between positrons, antiprotons, and normal matter in a trap well suited for laser spectroscopy.

ACKNOWLEDGMENTS

The authors thank M. Hori for his important contributions to the design and implementation of the experiment, N. Leefer for helpful discussions, K. Krimmel for his contribution in the early stages of the experiment, L. Cong for his help with the theoretical calculations, and R. Folman for his original proposal of "antimatter on a chip." M.H. thanks the Czech Science Foundation (GAČR Grant No. GA24-10992S) for support. N.V.L. thanks the Charles University Grant Agency (GAUK Grant No. 131224), and the Czech Ministry of Education, Youth, and Sports (Project No. QM4ST, ID No. EH22_008/0004572) for support. This work is supported by the National Natural Science Foundation of China (Grant No. 12405264). The study is supported in part by DFG Project ID No. 390831469: EXC 2118 (PRISMA+ Cluster of Excellence), the DFG project TACTICa (ID No. 495729045), and the project "Quantum Sensing for Fundamental Physics (QS4Physics)" funded by the Innovation Pool of the research field Helmholtz Matter of the Helmholtz Association.

DATA AVAILABILITY

The data that support the findings of this article are not publicly available. The data are available from the authors upon reasonable request.

APPENDIX: EMT CALIBRATION

As described in Sec. II B, the detection chain includes a Hamamatsu R596 electron multiplier tube (EMT), an Ortec 142PC charge-sensitive preamplifier (CSP), and a CAEN 5770 digitizer. Each primary electron or ion entering the EMT produces on the order of 10^6 electrons at the output.

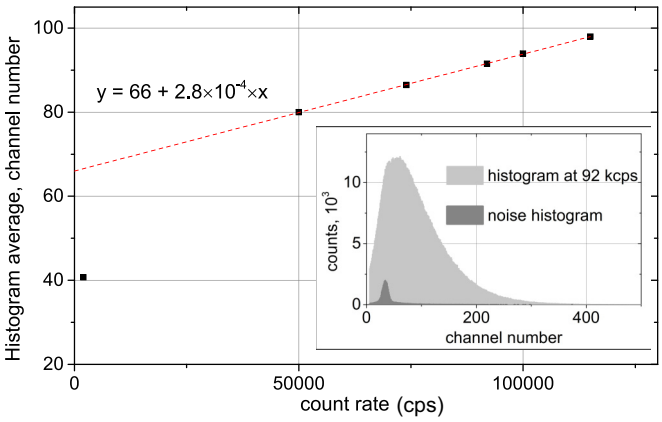

FIG. 13. Calibration of the detection chain in the case of electron detection. Black squares: histogram averages after 10^6 repetitions; red dashed line: linear approximation. Inset: a histogram of the EMT + CSP readout at a 92-cps count rate and a histogram of detector noise, with an acquisition time of 30 s.

The resulting charge pulse is amplified by the CSP and then counted as a detection event, whose voltage amplitude is measured using the 14-bit digitizer. EMT pulses resulting from single-electron events exhibit a Poisson-like amplitude distribution due to the statistical nature of secondary-electron emission [48]. We denote this single-electron response by P_1. If two electrons arrive at the EMT simultaneously or within the pileup time of the digitizer, they are counted as a single event and produce a pulse with double amplitude distribution P_2. When the number of electrons per detection event varies during the acquisition time, the resulting pulse-amplitude histogram consists of multiple overlapping distributions: $P_n = P_1 + P_2 + \cdots$, as shown in the inset of Fig. 13. The average number of electrons per detection event can then be calculated as $N = \bar{P}_n/\bar{P}_1$

To determine $\bar{P}_1$, we employ a simple model-independent approach. The digitizer is switched to the continuous-detection mode with internal triggering. Electrons are continuously produced by photoionization, whereas the quadrupole trapping field and extraction pulses are turned off. The typical EMT and holder potentials are applied so that most of the electrons produced hit the first dynode. We assume that the arrival of the electron in the EMT follows a Poisson distribution with an average interval of 1/cps, with cps being the number of detection events per second. In a specific range of count-rate values, the experimental distribution P can be written as a linear function on cps: $P(\text{cps}) = P_b + P_1 + aP_2 \times \text{cps}$, where P_b is the background noise and a is the weight of two-electron events. Then $\bar{P}(\text{cps}) = \bar{P}_b + \bar{P}_1 + a\bar{P}_2 \times \text{cps}$. By subtracting noise and extrapolating $\bar{P}(\text{cps})$ from the linear region to the zero count rate, we find $\bar{P}_1$. We vary the count rate from 50 to 115 kcps and determine the single-electron peak average $\bar{P}_1$ is in channel 66 ± 0.2. A similar approach is applied for the ions. The main source of uncertainty in this approach is the difference between the measured detection-event count rate and the true electron count rate. According to our estimation, this systematic error can be as high as 20%.

[1] S. A. McLuckey and J. L. Stephenson, Ion/ion chemistry of high-mass multiply charged ions, Mass Spectrom. Rev. **17**, 369 (1998).

[2] H. Dehmelt, Economic synthesis and precision spectroscopy of anti-molecular hydrogen ions in Paul trap, Phys. Scr. **1995**, 423 (1995).

[3] N. Leefer, K. Krimmel, W. Bertsche, D. Budker, J. Fajans, R. Folman, H. Häffner, and F. Schmidt-Kaler, Investigation of two-frequency Paul traps for antihydrogen production, Hyperfine Interact. **238**, 12 (2017).

[4] D. Trypogeorgos and C. J. Foot, Cotrapping different species in ion traps using multiple radio frequencies, Phys. Rev. A **94**, 023609 (2016).

[5] C. J. Foot, D. Trypogeorgos, E. Bentine, A. Gardner, and M. Keller, Two-frequency operation of a Paul trap to optimize confinement of two species of ions, Int. J. Mass Spectrom. **430**, 117 (2018).

[6] D. T. Snyder and R. G. Cooks, Ion isolation in a linear ion trap using dual resonance frequencies, J. Am. Soc. Mass Spectrom. **27**, 1906 (2016).

[7] M. Amoretti, *et al.*, Production and detection of cold antihydrogen atoms, Nature (London) **419**, 456 (2002).

[8] G. B. Andresen, *et al.*, Trapped antihydrogen, Nature (London) **468**, 673 (2010).

[9] M. Ahmadi, *et al.*, Antihydrogen accumulation for fundamental symmetry tests, Nat. Commun. **8**, 681 (2017).

[10] C. Smorra, F. Abbass, D. Schweitzer, M. Bohman, J. Devine, Y. Dutheil, A. Hobl, B. Arndt, B. Bauer, J. Devlin, Y. Yamazaki, and S. Ulmer, BASE-STEP: A transportable antiproton reservoir for fundamental interaction studies, Rev. Sci. Instrum. **94**, 113201 (2023).

[11] M. Leonhardt, *et al.*, Proton transport from the antimatter factory of CERN, Nature (London) **641**, 871 (2025).

[12] T. Aumann, *et al.*, PUMA, antiproton unstable matter annihilation, Eur. Phys. J. A **58**, 88 (2022).

[13] T. Leopold, S. A. King, P. Micke, A. Bautista-Salvador, J. C. Heip, C. Ospelkaus, J. R. Crespo López-Urrutia, and P. O. Schmidt, A cryogenic radio-frequency ion trap for quantum logic spectroscopy of highly charged ions, Rev. Sci. Instrum. **90**, 073201 (2019).

[14] A. Osada, K. Taniguchi, M. Shigefuji, and A. Noguchi, Feasibility study on ground-state cooling and single-phonon readout of trapped electrons using hybrid quantum systems, Phys. Rev. Res. **4**, 033245 (2022).

[15] K. Taniguchi and A. Noguchi, Image current detection of electrons in a room-temperature Paul trap, Phys. Rev. A **112**, 022420 (2025).

[16] R. Akbari, *et al.*, Be^+ assisted, simultaneous confinement of more than 15000 antihydrogen atoms, Nat. Commun. **16**, 10106 (2025).

[17] J. Walz, S. B. Ross, C. Zimmermann, L. Ricci, M. Prevedelli, and T. W. Hänsch, Combined trap with the potential for antihydrogen production, Phys. Rev. Lett. **75**, 3257 (1995).

[18] A. Pahl, K. Eikema, J. Walz, and T. Hänsch, Combined trap for laser stimulated recombination, Hyperfine Interact. **127**, 181 (2000).

[19] P. Blumer, *et al.*, Positron accumulation in the GBAR experiment, Nucl. Instrum. Methods Phys. Res. A **1040**, 167263 (2022).

[20] L. Canetti, M. Drewes, and M. Shaposhnikov, Matter and antimatter in the universe, New J. Phys. **14**, 095012 (2012).

[21] M. Ahmadi, B. Alves, C. Baker, W. Bertsche, A. Capra, C. Carruth, C. Cesar, M. Charlton, S. Cohen, R. Collister, D. V. D. Werf, and J. Wurtele, Characterization of the 1s-2s transition in antihydrogen, Nature (London) **557**, 71 (2018).

[22] M. Ahmadi, B. Alves, C. Baker, W. Bertsche, A. Capra, C. Carruth, C. Cesar, M. Charlton, S. Cohen, R. Collister, D. van der Werf, and J. Wurtele, Investigation of the fine structure of antihydrogen, Nature (London) **578**, 375 (2020).

[23] K. Khabarova, A. Golovizin, and N. Kolachevsky, Antihydrogen and hydrogen: Search for the difference, Symmetry **15**, 1603 (2023).

[24] M. Hori, A. Sótér, D. Barna, A. Dax, R. Hayano, S. Friedreich, B. Juhász, T. Pask, E. Widmann, D. Horváth, L. Venturelli, and N. Zurlo, Two-photon laser spectroscopy of antiprotonic helium and the antiproton-to-electron mass ratio, Nature (London) **475**, 484 (2011).

[25] G. Gabrielse, A. Khabbaz, D. S. Hall, C. Heimann, H. Kalinowsky, and W. Jhe, Precision mass spectroscopy of the antiproton and proton using simultaneously trapped particles, Phys. Rev. Lett. **82**, 3198 (1999).

[26] S. Ulmer, C. Smorra, A. Mooser, K. Franke, H. Nagahama, G. Schneider, T. Higuchi, S. V. Gorp, K. Blaum, Y. Matsuda, J. Walz, and Y. Yamazaki, High-precision comparison of the antiproton-to-proton charge-to-mass ratio, Nature (London) **524**, 196 (2015).

[27] R. J. Hughes and B. I. Deutch, Electric charges of positrons and antiprotons, Phys. Rev. Lett. **69**, 578 (1992).

[28] R. S. Van Dyck, Jr., P. B. Schwinberg, and H. G. Dehmelt, New high-precision comparison of electron and positron g factors, Phys. Rev. Lett. **59**, 26 (1987).

[29] J. Disciacca, M. Marshall, K. Marable, G. Gabrielse, S. Ettenauer, E. Tardiff, R. Kalra, D. Fitzakerley, M. C. George, E. A. Hessels, C. H. Storry, M. Weel, D. Grzonka, W. Oelert, and T. Sefzick, One-particle measurement of the antiproton magnetic moment, Phys. Rev. Lett. **110**, 130801 (2013).

[30] G. Gabrielse, X. Fei, L. Haarsma, S. L. Rolston, R. Tjoelker, T. A. Trainor, H. Kalinowsky, J. Haas, and W. Kells, First capture of antiprotons in an ion trap: Progress toward a precision mass measurement and antihydrogen, Phys. Scr. **1988**, 36 (1988).

[31] G. Gabrielse, X. Fei, L. A. Orozco, R. L. Tjoelker, J. Haas, H. Kalinowsky, T. A. Trainor, and W. Kells, Cooling and slowing of trapped antiprotons below 100 meV, Phys. Rev. Lett. **63**, 1360 (1989).

[32] V. V. Flambaum, C. Harabati, V. A. Dzuba, and G. F. Gribakin, Periodic table of positronic atoms, J. Phys.: Conf. Ser. **635**, 052028 (2015).

[33] C. Harabati, V. A. Dzuba, and V. V. Flambaum, Identification of atoms that can bind positrons, Phys. Rev. A **89**, 022517 (2014).

[34] D. S. Bykov, L. Dania, F. Goschin, and T. E. Northup, A nanoparticle stored with an atomic ion in a linear Paul trap, Phys. Rev. Lett. **135**, 213602 (2025).

[35] C. Matthiesen, Q. Yu, J. Guo, A. M. Alonso, and H. Häffner, Trapping electrons in a room-temperature microwave Paul trap, Phys. Rev. X **11**, 011019 (2021).

[36] N. Daniilidis, D. J. Gorman, L. Tian, and H. Häffner, Quantum information processing with trapped electrons and superconducting electronics, New J. Phys. **15**, 073017 (2013).

[37] S. Kotler, R. W. Simmonds, D. Leibfried, and D. J. Wineland, Hybrid quantum systems with trapped charged particles, Phys. Rev. A **95**, 022327 (2017).

[38] N. Lausti, V. Kumar, and M. Hejduk, Electrical properties of a coaxial electron-ion trap, in *WDS'23 Proceedings of Contributed Papers—Physics*, edited by J. Šafránková and J. Pavlů (Matfyzpress, Prague, 2023), pp. 191–196.

[39] J. M. Wells, P. A. Chrisman, and S. A. McLuckey, "Dueling" ESI: Instrumentation to study ion/ion reactions of electrospray-generated cations and anions, J. Am. Soc. Mass Spectrom. **13**, 614 (2002).

[40] S. Gulde, D. Rotter, P. Barton, F. Schmidt-Kaler, R. Blatt, and W. Hogervorst, Simple and efficient photo-ionization loading of ions for precision ion-trapping experiments, Appl. Phys. B **73**, 861 (2001).

[41] F. Major, V. Gheorghe, and G. Werth, *Charged Particle Traps*, Springer Series on Atomic, Optical, and Plasma Physics (Springer, 2005), Vol. 37.

[42] D. Gerlich, Inhomogeneous RF fields: A versatile tool for the study of processes with slow ions, in *Advances in Chemical Physics*, edited by C.-Y. Ng, M. Baer, I. Prigogine and S. A. Rice (Wiley, 1992).

[43] K.-Y. Lin, G. H. Low, and I. L. Chuang, Effects of electrode surface roughness on motional heating of trapped ions, Phys. Rev. A **94**, 013418 (2016).

[44] B. Ou, J. Zhang, X. Zhang, Y. Xie, T. Chen, C. Wu, W. Wu, and P. Chen, Optimization of parameters of a surface-electrode ion trap and experimental study of influences of surface on ion lifetime, Sci. China: Phys. Mech. Astron. **59**, 123011 (2016).

[45] S. J. Simeth, A. Müller, J. Müller, B. Lekitsch, M. Reininghaus, and F. Schmidt-Kaler, Selective laser-induced etching for 3D ion traps, Proc. SPIE **12409**, 1240902 (2023).

[46] Z. D. Romaszko, S. Hong, M. Siegele, R. K. Puddy, F. R. Lebrun-Gallagher, S. Weidt, and W. K. Hensinger, Engineering of microfabricated ion traps and integration of advanced on-chip features, Nat. Rev. Phys. **2**, 285 (2020).

[47] J. R. Danielson, D. H. E. Dubin, R. G. Greaves, and C. M. Surko, Plasma and trap-based techniques for science with positrons, Rev. Mod. Phys. **87**, 247 (2015).

[48] R. Saldanha, L. Grandi, Y. Guardincerri, and T. Wester, Model independent approach to the single photoelectron calibration of photomultiplier tubes, Nucl. Instrum. Methods Phys. Res. Sect. A **863**, 35 (2017).